

The Integrated Sachs-Wolfe Signal from BOSS Super-Structures

Benjamin R. Granett^{1*}, András Kovács², Adam J. Hawken¹

¹*Istituto Nazionale di Astrofisica - Osservatorio Astronomico di Brera, Via E. Bianchi 46, 23807 Merate, Italy*

²*Institut de Física d'Altes Energies, Universitat Autònoma de Barcelona, E-08193 Bellaterra (Barcelona), Spain*

8 November 2021

ABSTRACT

Cosmic structures leave an imprint on the microwave background radiation through the integrated Sachs-Wolfe effect. We construct a template map of the linear signal using the SDSS-III Baryon Acoustic Oscillation Survey at redshift $0.43 < z < 0.65$. We verify the imprint of this map on the Planck CMB temperature map at the 97% confidence level and show consistency with the density-temperature cross-correlation measurement. Using this ISW reconstruction as a template we investigate the presence of ISW sources and further examine the properties of the Granett-Neyrinck-Szapudi supervoid and supercluster catalogue. We characterise the three-dimensional density profiles of these structures for the first time and demonstrate that they are significant structures. Model fits demonstrate that the supervoids are elongated along the line-of-sight and we suggest that this special orientation may be picked out by the void-finding algorithm in photometric redshift space. We measure the mean temperature profiles in Planck maps from public void and cluster catalogues. In an attempt to maximise the stacked ISW signal we construct a new catalogue of super-structures based upon local peaks and troughs of the gravitational potential. However, we do not find a significant correlation between these structures and the CMB temperature.

Key words: cosmological parameters, observations, large-scale structure of Universe, methods: statistical

1 INTRODUCTION

Striking correlations have been observed between cosmic super-structures and the cosmic microwave background (CMB). Most prominently Granett, Neyrinck & Szapudi (2008) (hereafter GraNeSz) reported a 4σ detection of voids and clusters at redshift $z = 0.5$ identified in the Sloan Digital Sky Survey (SDSS) imprinted on the CMB as $10\mu\text{K}$ cold and hot spots on 4° scales. Additionally, there is evidence for a supervoid at redshift $z = 0.2$ aligned with the Cold Spot suggesting a causal relationship (Szapudi et al. 2015). While these findings may be statistically significant, the physical mechanism producing the correlation has yet to be determined. The leading candidate has been the late-time integrated Sachs-Wolfe effect (Sachs & Wolfe 1967; Rees & Sciama 1968). However, the scale of the temperature correlation is inconsistent with the expectation in the standard ΛCDM cosmological model for typical supervoid and superclusters (Cai et al. 2010; Nadathur, Hotchkiss & Sarkar 2012; Hernández-Monteagudo & Smith 2013; Flender, Hotchkiss & Nadathur 2013; Nadathur & Hotchkiss 2014; Hotchkiss

et al. 2015; Aiola, Kosowsky & Wang 2015) and cannot fully explain the Cold Spot (Nadathur et al. 2014; Zibin 2014). Moreover, the signal-to-noise ratio for the ISW measurement with SDSS galaxies is expected to be ~ 1.7 (Hernández-Monteagudo et al. 2014), while a full-sky survey to redshift 2 can reach a maximum $S/N \sim 7$ (Afshordi 2004). Thus the anomalous contribution from individual sources may point to new physics.

The ISW signal is challenging to measure because the amplitude is an order of magnitude below the primary temperature anisotropies. It may be detected by cross-correlating galaxy tracers with the cosmic microwave background over the sky or at the locations of particular super-structures (Nishizawa (2014) offers a review). In flat cosmologies the ISW signal is sensitive to dark energy (Crittenden & Turok 1996) and provides important constraints for modified gravity models (Giannantonio et al. 2010) as well as for primordial non-Gaussianity (Afshordi & Tolley 2008). The signal may be enhanced by adding constraints from the primordial polarisation of the CMB (Frommert & Enßlin 2009). It may also be independently estimated by correlating against the infrared background (Ilić et al. 2011)

* E-mail: ben.granett@brera.inaf.it

and 21cm brightness maps (Raccanelli et al. 2015) adding to the detection significance.

Since the ISW effect is subtle, analyses can be prone to over-fitting and suffer from the ‘look elsewhere’ effect (Peiris 2014). It is a particular problem for the study of ISW sources since the physical nature of supervoid and supercluster structures identified in galaxy surveys is not well-known and there is not a clear expectation for the signal. Numerical N-body simulations have been used to predict the ISW anisotropy arising from voids and clusters and to determine the optimal detection filters (Cai et al. 2010, 2014; Hotchkiss et al. 2015). Guided by these results, attempts to reproduce the GraNeSz measurement with other super-structure catalogues have lead to only marginal or null detections (Kovács & Granett 2015; Hotchkiss et al. 2015; Nadathur & Hotchkiss 2014; Cai et al. 2014; Ilić, Langer & Douispis 2013). These studies would suggest that the GraNeSz detection arises from a different physical mechanism or is a statistical fluke.

However, an important piece of the puzzle remains out of place. To date, there has been no characterisation of the three-dimensional properties of the GraNeSz structures. Analyses have used superstructure catalogues derived from spectroscopic redshift catalogues employing variations of the watershed algorithm based on the ZOBOV code (Neyrinck 2008; Neyrinck, Gnedin & Hamilton 2005). The GraNeSz super-structures were identified with a photometric redshift catalogue and the correspondence between the void finding techniques is not yet clear. As pointed out by Kovács & Granett (2015) the GraNeSz supervoids do not correlate with the voids identified in three-dimensions with the watershed algorithm.

Besides the use of N-body simulations, an alternative empirical approach is possible: we may predict the ISW signal directly from galaxy surveys, without modelling individual structures. All-sky reconstructions of the ISW signal assuming linear dynamics have already proven to be useful for investigating possible large-scale anomalies on the CMB (Maturi et al. 2007; Granett, Neyrinck & Szapudi 2009; Francis & Peacock 2010; Rassat, Starck & Dupé 2013; Manzotti & Dodelson 2014).

Previously, the GraNeSz sources were investigated using an ISW map constructed based upon the photometric luminous red galaxy (LRG) sample at redshift $z = 0.5$ (Granett, Neyrinck & Szapudi 2009). Although the map contained hot and cold spots corresponding to the super-structures, the amplitude of the effect was slight, with only $\Delta T^{cluster} - \Delta T^{void} = 0.08 \pm 0.1 \mu\text{K}$. This result seemingly contradicted the claim that the $10 \mu\text{K}$ anisotropy was arising from the linear ISW effect. To resolve this question we are motivated to improve the fidelity of the ISW reconstruction by building it using a galaxy sample with measured spectroscopic redshifts.

We are now in a position to carry out these investigations using the SDSS-III Baryon Acoustic Oscillation Survey CMASS spectroscopic sample which covers the sky area and redshift range of the original GraNeSz analysis (Alam et al. 2015; Bolton et al. 2012). In general, the BOSS sample is interesting for ISW studies because, due to the volume dependence, the sensitivity to ISW is expected to peak at redshift $z \sim 0.5$ (Afshordi 2004). Analyses have shown the cross-correlation measurements of the luminous red galaxy

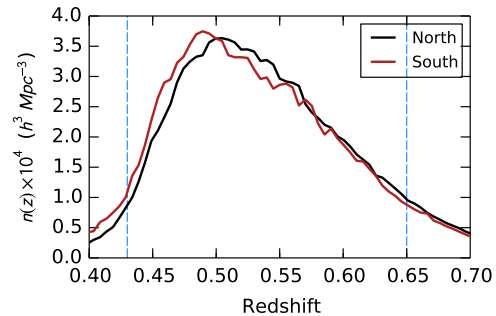


Figure 1. Redshift distribution of the CMASS samples in the North and South Galactic cap fields. The vertical dashed lines indicate the redshift ranges used in this study.

sample in the North Galactic cap show an excess signal (Ho et al. 2008; Giannantonio et al. 2008; Granett, Neyrinck & Szapudi 2009), despite low significance (Sawangwit et al. 2010). The complete photometric BOSS sample was analysed by Hernández-Monteagudo et al. (2014) and Giannantonio et al. (2014).

Galaxies in the CMASS sample have spectroscopic redshift measurements, as opposed to photometric redshifts in the photometric LRG samples used previously. While precise redshift measurements are not necessary for cross-correlation measurements using the projected galaxy density field, they are necessary to reconstruct the three-dimensional potential.

We begin this article by detailing the spectroscopic CMASS sample in Sec. 2 including our corrections for the known systematic inhomogeneities. In Sec. 3 we then describe the procedure to estimate the underlying density field, the three-dimensional gravitational potential and the linear ISW map. We validate the ISW map using the template fit statistic against the Planck CMB temperature map. In Sec. 4 we carry out the consistency check between the ISW map and the angular galaxy-CMB cross correlation function. In Sec. 5 we characterise the GraNeSz super-structures by fitting the three-dimensional density profiles. In Sec. 6 we address our main concerns, ISW sources. We characterise the three-dimensional properties of the GraNeSz structures using the CMASS sample and estimate their contribution to the linear ISW effect using the ISW map. For comparison, we consider the publicly available void catalogue by Sutter et al. (2014). We also construct a new super-structure catalogue based upon the local peaks and troughs of the three-dimensional gravitational potential that should be ideal ISW sources. We conclude in Sec. 7 with suggestions for future investigations.

2 DATA

2.1 Galaxy sample

We use the constant stellar mass (CMASS) galaxy sample from the Sloan Digital Sky Survey-III (SDSS-III) Baryon Oscillation Spectroscopic Survey (BOSS) Data Release 12 (Alam et al. 2015; Bolton et al. 2012). We extract the photometric parent catalog from the targeting catalog for

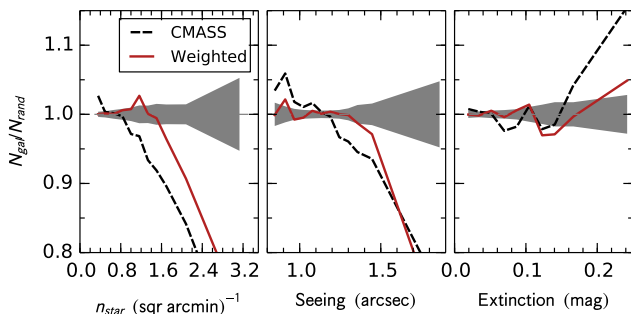


Figure 2. The mean number density of the CMASS sample with respect to a uniform random catalogue as a function of stellar density (left), seeing (center) and Galactic extinction (right). The dashed line shows the systematic trends present in the catalogue. After applying corrective weights we find the trends indicated by the solid lines. The shaded regions indicate the 68% uncertainty range for Poisson counts.

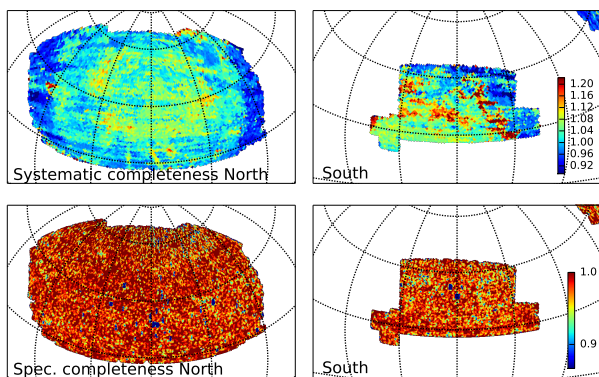


Figure 3. The CMASS completeness maps for the North and South galactic caps. The top frames show the systematic completeness correlated with stellar density, seeing, extinction and galaxy surface brightness. The bottom frames show the spectroscopic completeness.

the ninth and final run. This provides a uniform photometric selection over the full survey. The targets are selected with the CMASS target selection flag and fibre magnitude limit (`boss_target1&BOSS_CMASS>0`). We then look up the redshifts of these sources in the spectroscopic objects database selecting all primary objects (`scienceprimary=1`). We match the photometric and spectroscopic catalogs using position on the sky with a match radius of 1 arcsec. We take the BOSS galaxy redshift estimate `z_noqso` when successfully measured (`zwarning_noqso=0`). If the BOSS redshift estimate is not available, we take the legacy redshift measurement as long as it was successfully measured (`zwarning=0`).

The CMASS sample covers two discontinuous fields in the Northern and Southern Galactic caps. We use the survey mask that characterises the CMASS targeting catalogue. We extract the polygons from the mask that correspond to the BOSS survey runs (2,5,7,8 and 9) based upon the chunk identifiers. We exclude sources that fall within the photometric quality, bright star and centre post masks. We use the Mangle code (Swanson et al. 2008) to carry out these tasks.

The spectroscopic redshift distribution of the final catalogue is shown in Fig. 1. When estimating the underlying density field we combine two subsamples with redshift ranges (I) $0.43 < z < 0.55$ and (II) $0.55 < z < 0.65$ described in Table. 1. We consider separately the Northern and Southern Galactic cap fields.

2.2 Survey completeness

The parent catalog from which CMASS targets were selected is known to be inhomogeneous. Seeing conditions, stellar density and Galactic extinction were found to impact the number density of galaxies with a dependence on galaxy surface brightness (Ho et al. 2012; Ross et al. 2012). Here, we quantify those effects and compute corrective weights.

We first estimate the spectroscopic sampling rate. The number of sources in the photometric target sample is given by N_{targ} of which N_{obs} have measured redshifts. After classifying as stars or galaxies we have $N_{obs} = N_{gal} + N_{star}$. We then define the spectroscopic completeness for galaxies as $c_{spec} = N_{gal}/(N_{targ} - N_{star})$. The completeness is computed for each galaxy by counting the number of sources within a radius of $R = 30$ arcmin. From the completeness we derive a weight for each galaxy: $w_{spec,i} = 1/c_{spec,i}$. The map of the spectroscopic completeness is shown in Fig. 3. At redshift $z = 0.5$, 30 arcmin on the sky corresponds to a comoving separation of $11h^{-1}$ Mpc, so we do not expect effects correlated on the scale of the detector to influence large-scale modes in the density field.

To address possible large-scale systematic effects, we construct maps of each potential source. We selected stars as in Anderson et al. (2014) by taking sources with $17.5 < i_{dered} < 19.9$ from the SDSS `star` database table to create an angular density healpix map (Górski et al. 2005). We build a map of the seeing taking the i -band FWHM of the PSF from the target photometric catalog averaging the seeing values within Healpix cells. We create a galactic extinction map in the same way using the i band extinction. We also use the $2''$ fibre magnitude as a proxy for galaxy surface brightness.

We compare the density of galaxies to the density of unclustered random points distributed over the survey area. Each random point has an associated stellar density, seeing and extinction assigned based upon the sky coordinate and a surface brightness drawn independently from the observed distribution. Fig. 2 shows the normalised galaxy density with respect to randoms as a function of each potential systematic. There is a deficit of sources in regions with high stellar density or poor seeing while we find an excess of sources in regions with high values of reddening.

The completeness depends on a four-dimensional parameter space of fibre magnitude, stellar density, seeing and extinction. We develop a non-parametric approach using the K -means algorithm to adaptively bin the data. We use the algorithm to construct $K = 500$ adaptive bins each associated with roughly 2000 unique galaxies. This is carried out using a rank-order distance metric to standardise the parameters.

We compute the completeness in each bin by counting the weighted number of galaxies with respect to the number of randoms: $c_{sys} = \sum_{i=1}^N w_{spec,i} \alpha / N_r$. The completeness is then assigned to each galaxy in the bin. The map of the systematic completeness is shown in the top row of Fig. 3.

Sample		Number	Median z	Galaxy bias
$0.43 < z < 0.55$	North	309900	0.503	1.94 ± 0.01
	South	109793	0.499	1.97 ± 0.01
$0.55 < z < 0.65$	North	218311	0.590	2.15 ± 0.01
	South	77872	0.590	2.18 ± 0.02

Table 1. Galaxy samples and best-fit bias parameters. The bias parameters are derived after fixing the amplitude of the matter power spectrum with $\sigma_8 = 0.8$ under the fiducial cosmology given in the text.

After weighting the density field by the inverse of the systematic completeness, we find the trends given by the solid red curve in Fig. 2. The correlations are reduced although we still see a significant dependence at the parameter extremes. However, the last bin in the plots is an average over 150 cells, so it represents only 1% of the total area. The trends shown in Fig. 2 are in good agreement with those published in Ross et al. (2012) which gives us confidence in our independent methodology. The total selection function is given by the product of the spectroscopic and systematic completeness fractions: $c_i = c_{spec,i} \times c_{sys,i}$.

2.3 CMB maps

The second data release from the Planck mission provides both temperature and polarisation maps (Planck Collaboration et al. 2015a). We use the foreground cleaned SMICA temperature map downgraded to 1° resolution ($n_{side} = 64$) (Planck Collaboration et al. 2015b). The polarisation data may also be used to help separate the late-time and primordial temperature anisotropies. However, as of the latest release, the polarisation data is not available on large scales, harmonic $\ell < 40$, making the gain in the joint analysis negligible (Planck Collaboration et al. 2015c). Thus, we proceed with the analysis using only the temperature maps.

3 ISW MAPS

A prediction of the linear ISW signal may be obtained from the galaxy density field by employing the Poisson equation (Granett, Neyrinck & Szapudi 2009). We use a Wiener filter to estimate the underlying matter density field and correct for survey completeness. The Wiener filter gives the minimum-variance estimate of the density field. In the Bayesian formulation it corresponds to the maximum a-posteriori solution assuming a Gaussian likelihood and prior, assumptions that hold for the galaxy field on large scales.

Our method is based on the Gibbs sampler developed to reconstruct the underlying density field of the VIPERS galaxy sample (Granett, B. R. et al. 2015) with adjustments to accommodate the CMASS sample. We upweight the galaxies using the inverse of the completeness as described above. We divide the CMASS sample into two subsamples by redshift: $0.43 < z < 0.55$ and $0.55 < z < 0.65$. The subsamples are combined to jointly estimate a single density field, but we allow the relative galaxy biases to vary. The weighted number of galaxies from each subsample is assigned over a comoving cartesian grid with cubic cells

$10h\text{Mpc}^{-1}$ on a side. We process separately the Northern and Southern Galactic caps. The North is embedded into a cube with 256 cells on a side while the South fits in a slightly smaller box with size 200 cells. The number of galaxies in a given cell indexed by i may be related to an underlying over-density field δ_g ,

$$N_i = w_i \bar{N}_i (1 + \delta_{g,i}). \quad (1)$$

The mean number density of the cell is \bar{N}_i and the selection function is w_i . The selection function is estimated from the normalised number of random points falling in the given cell. It includes the angular mask. The redshift distribution is contained in \bar{N}_i . The expected shot noise in the cell is $\sigma_i^2 = \alpha w_i \bar{N}_i$, where α accounts for the completeness weights.

As in Granett, B. R. et al. (2015) our data model includes a constant galaxy bias and the redshift distribution is left free. However, in this analysis we fix the power spectrum to the fiducial model computed with CLASS to reduce the convergence time of the Gibbs sampler. The non-linear power spectrum is computed using Halofit (Takahashi et al. 2012) with the fiducial parameter set ($h = 0.6774$, $\Omega_m = 0.3089$, $\sigma_8 = 0.80$) at effective redshift $z_{ref} = 0.55$). Use of the non-linear power spectrum aids in accurately recovering small-scale structures. Instead if we used the purely linear power spectrum the field would be unnecessarily smoothed. We apply the Wiener filter isotropically in redshift space and so we use the monopole of the power spectrum estimated using the dispersion model with distortion parameters $\beta = 0.375$ and $\sigma_v = 400\text{km/s}$ (Peacock & Dodds 1994; Cabré & Gaztañaga 2009).

We find that the Gibbs sampler converges after 10 steps. To produce realisations of the density field we ran 7 chains, each with 500 steps. The constraints on the bias parameters are listed in Table 1.

From the density field we may estimate the gravitational potential using the Poisson equation in Fourier space,

$$k^2 \Phi(\vec{k}) = -\frac{3}{2} H_0^2 \Omega_m (1+z) \delta(\vec{k}). \quad (2)$$

In doing so, we scale δ with the linear growth factor to a common epoch: $\delta(z_{ref}) = \delta(z) D(z_{ref}) / D(z)$. This computation is carried out via the FFT algorithm.

The ISW signal is an integral over the time-derivative of the potential along the line-of-sight,

$$T_{ISW} = -T_{CMB} \frac{2}{c^2} \int \frac{d\Phi}{d\tau} d\tau. \quad (3)$$

However, this is simplified using the linear prediction, that is, $d\Phi/d\tau \propto d(1+z)D(z)/d\tau$, to obtain,

$$T_{ISW}(\theta, \phi) = -T_{CMB} \frac{2}{c^2} \frac{1}{(1+z_{ref})D(z_{ref})} \times \sum_i \Phi(\theta, \phi, r_i) \left[\frac{d(1+z)D(z)}{dr} \right]_{r_i} \Delta r \quad (4)$$

which represents a projection over the potential field with a given kernel. After projecting the potential along the line-of-sight of the North and South samples we find the ISW maps shown in Fig. 4. In Appendix A we compare this map with the reconstruction from Granett, Neyrinck & Szapudi (2009) which was based upon a photometric luminous red galaxy sample over a similar redshift range in the Northern field.

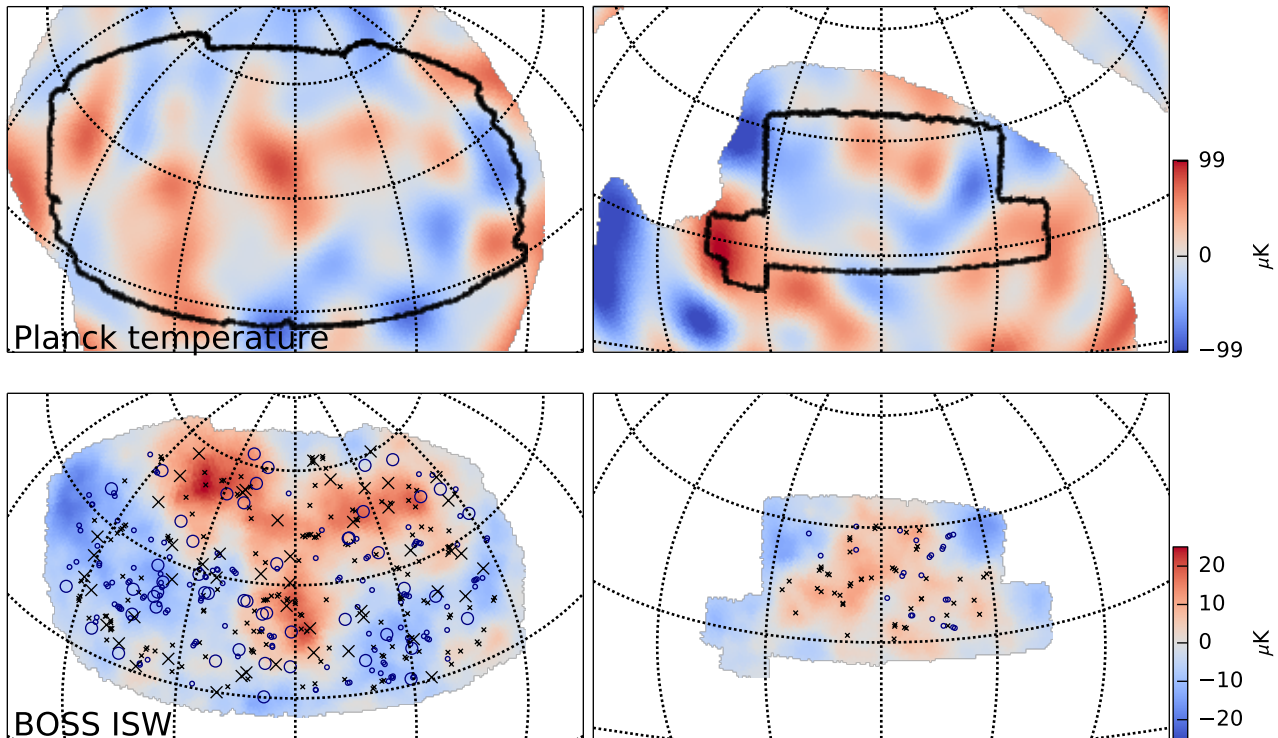


Figure 4. Top row: CMB maps after low-pass filtering $\ell < 20$. Bottom row: ISW maps. Cross symbols mark the angular position of local maxima of the gravitational potential and open circles mark local minima more than 10° from survey boundaries. The locations of GrNeSz supervoids and superclusters are indicated by the large open circles and crosses. The CMASS survey boundary is overlotted in black over the CMB temperature maps.

3.1 Template fit

The observed CMB temperature map may be written as a sum of components including the primary temperature T_{primary} , the ISW signal T_{ISW} and the uncorrelated foreground contribution $T_{\text{foreground}}$

$$T_{\text{CMB}} = T_{\text{primary}} + T_{\text{foreground}} + \lambda T_{\text{ISW}} \quad (5)$$

The maximum likelihood estimator for the amplitude parameter λ is

$$\hat{\lambda} = \frac{T_{\text{CMB}} C^{-1} T_{\text{ISW}}}{T_{\text{ISW}} C^{-1} T_{\text{ISW}}}. \quad (6)$$

The variance is given by

$$\sigma^2 = (T_{\text{ISW}} C^{-1} T_{\text{ISW}})^{-1}. \quad (7)$$

The covariance matrix C is given by $C = \langle (T_{\text{primary}} + T_{\text{foreground}})^2 \rangle$. We use the best fitting temperature power spectrum model from Planck computed using CLASS. In pixel space, the covariance matrix is

$$C_{ij} = \sum_l \frac{2l+1}{4\pi} C_l W_l^2 P_l(\cos \theta_{ij}), \quad (8)$$

where P_l is the Legendre polynomial and θ_{ij} is the angular separation between two healpix cells indexed by i and j . The window function W_l is set by the Healpix pixelization at $n_{\text{side}} = 64$. At this resolution we neglect the beam and instrument noise.

A correction to the covariance must be added to address the fact that we estimate the mean of the distribution from the sample itself. The covariance is $C'_{ij} =$

$\langle (x_i - \bar{x})(x_j - \bar{x}) \rangle$ where \bar{x} is the mean pixel value within the survey: $\bar{x} = \frac{1}{N_{\text{pix}}} \sum_i x_i$. Expanding, this becomes $C'_{ij} = \langle x_i x_j \rangle - \frac{1}{N} \sum_\alpha \langle x_i x_\alpha \rangle - \frac{1}{N} \sum_\alpha \langle x_\alpha x_j \rangle + \frac{1}{N^2} \sum_\alpha \sum_\beta \langle x_\alpha x_\beta \rangle$.

The results of the template fit are presented in Table 2. Considering the Northern map, we find that the ISW amplitude $\lambda = 0.41$ with signal-to-noise 2.1. The Southern map gives no indication of a signal with an amplitude consistent with zero. In combination, we find $\lambda = 0.33 \pm 0.17$ giving a one-tailed p-value $p = 0.03$.

3.2 Discussion

The template fit amplitude gives the degree of agreement between the fluctuations observed on the CMB and those expected from the galaxy field through the linear ISW effect. If the ingredients of the model are correct we expect an amplitude of unity. The value less than 1 means that we have over-predicted the fluctuations on the CMB. Physically we may relate this to the amplitude of galaxy fluctuations through the bias parameter implying a galaxy bias larger than anticipated. The amplitude $\lambda = 0.4$ may be reconciled by increasing the bias by a factor of 2.5.

Previously, Granett, Neyrinck & Szapudi (2009) found a template fit amplitude greater than 1. In that work, it was found that the amplitude depended on the number density, redshift distribution and redshift uncertainty of the galaxy tracers and furthermore, that shot noise biases the amplitude low. Thus at this point, we do not draw conclusions

Field	ΔT_{ISW} Template fit			1-tail p
	λ	σ	λ/σ	
North	0.41	0.20	2.1	0.02
South	0.09	0.34	0.3	0.4
Combined	0.33	0.17	1.9	0.03
Field	C_ℓ^{ggT} Power spectrum fit			1-tail p
	A	σ	A/σ	
North	2.5	1.1	2.2	0.01
South	2.1	1.9	1.1	0.1
Combined	2.4	1.0	2.4	0.01
Clean North	0.7	1.1	0.6	0.3
Clean South	1.8	1.9	0.9	0.2
Clean Comb.	0.9	1.0	0.9	0.2

Table 2. The best-fit model template amplitudes for the ISW map and angular power spectrum measurements.

from the value of the amplitude and take the signal-to-noise ratio as confirmation of the validity of the map.

4 ANGULAR CROSS-CORRELATION

A standard probe of the ISW effect is the cross-correlation of galaxy density fields and CMB temperature maps. For SDSS luminous red galaxy data sets, previous studies found a moderately significant $2 - 2.5\sigma$ correlation with amplitudes higher than expected in the Λ CDM model (Ho et al. 2008; Giannantonio et al. 2008; Granett, Neyrinck & Szapudi 2009). Other studies reported ISW signals consistent with Λ CDM (Hernández-Monteaudo et al. 2014; Giannantonio et al. 2014).

We select CMASS galaxies in the redshift range $0.43 < z < 0.65$ and compute the projected density field on a Healpix grid with resolution 1° ($n_{\text{side}} = 64$). The selection function is estimated by assigning particles from the random catalogue in the same fashion. We then normalise the galaxy count map by the density randoms in each cell, setting to zero cells that are less than 50% complete.

4.1 Auto power-spectra

We compute harmonic-space power spectra, $C_\ell^{XY} = \langle a_{\ell m}^X a_{\ell m}^Y \rangle$, using the SpICE code (Chon et al. 2004) which properly accounts for the survey geometry. We first compute the auto-power spectrum of this map as a function of spherical harmonic index ℓ , C_ℓ^{gg} , shown in Fig. 5. We measure consistent values in our bins of width $\Delta\ell = 10$ in the Northern and Southern hemispheres. We thus analyse multipoles $\ell < 80$ since the theoretical S/N for an ISW signal in the Λ CDM model already converges at ~ 1.7 for $\ell \approx 60$ (Hernández-Monteaudo et al. 2014). For comparison, we overplot a model computed under best-fit Planck cosmological parameters ($h = 0.6774$, $\Omega_m = 0.3089$, $\sigma_8 = 0.80$) at effective redshift $z_{ref} = 0.55$. The constant galaxy bias $b_g = 2$ provides a good fit. The systematic weights alleviate the excess power on large-scales.

The fiducial model is given by the projection of the

r_v (h^{-1} Mpc)	Supervoids		
	α	q	σ_{los} (h^{-1} Mpc)
35.9 ± 3	1.7 ± 0.15	2.6 ± 0.4	76 ± 9
r_s (h^{-1} Mpc)	Superclusters		
	δ_c	q	σ_{los} (h^{-1} Mpc)
9.0 ± 3	167_{-85}^{+220}	$0.64_{-0.2}^{+0.3}$	79 ± 9

Table 3. Best fit parameters for GraNeSz supervoid and supercluster mean profiles with 68% confidence limits.

power spectrum in the plane-parallel limit:

$$C_\ell^{gg} = \int dr r^2 n(r)^2 b_g^2(r) \frac{D^2(r)}{D^2(z_{ref})} P\left(\frac{\ell+1/2}{r} | z_{ref}\right). \quad (9)$$

The redshift distribution is normalised such that $\int dr r^2 n(r) = 1$, $b(r)$ is the galaxy bias, $D(r)/D(z_{ref})$ is the growth factor that linearly evolves the field to redshift z_{ref} and P is the non-linear power spectrum estimated at redshift z_{ref} . We assume that the galaxy bias is constant over the redshift range of interest.

4.2 Cross power-spectra

Similarly, the expected angular power spectrum in the flat-sky limit, see Afshordi (2004), is an integral over the line-of-sight distance r ,

$$C_\ell^{\delta T} = T_{\text{CMB}} \frac{3H_0^2 \Omega_m b_g}{c^2} \frac{1}{(\ell+1/2)^2} \times \int dr r^2 n(r) \frac{d(1+z)D_1(z)}{dr} P\left(\frac{\ell+1/2}{r}\right), \quad (10)$$

where, $n(r) = \frac{dN(r)}{d^3z dV}$ is the galaxy selection function normalized by $\int r^2 \frac{d^3z dV}{dz dV} dr$, D_1 is the growth factor and $P\left(k = \frac{\ell+1/2}{r}\right)$ is the matter power spectrum at redshift z_{ref} .

In Fig. 5 we show the cross correlation between the galaxy density field and the CMB. We allow the amplitude of the model to be free with parameter A and find the best-fit value and uncertainty. We introduce the amplitude parameter A which has a distinct interpretation from the amplitude λ used in the template map fit. The value $A = 1$ would imply consistency with the Λ CDM expectation with the best-fit galaxy bias and $A > 1$ can be reconciled by increasing the galaxy bias. The fit results are summarised in Table 2. While systematic differences between the two hemispheres may affect our measurement (Giannantonio et al. 2014), we find consistent ISW signals for the Northern, Southern, and combined maps.

As a consistency test of the ISW map derived in Sec. 3, we subtract it from the Planck CMB temperature map and refer to this as the ISW cleaned map. Repeating the cross-correlation measurement, we find that the amplitude drops to $A = 0.9 \pm 1.0$ when the galaxy density map is cross correlated with the ISW cleaned CMB map. The match between the two methods is better for the Northern field, while a residual remains in the South at the 1σ level.

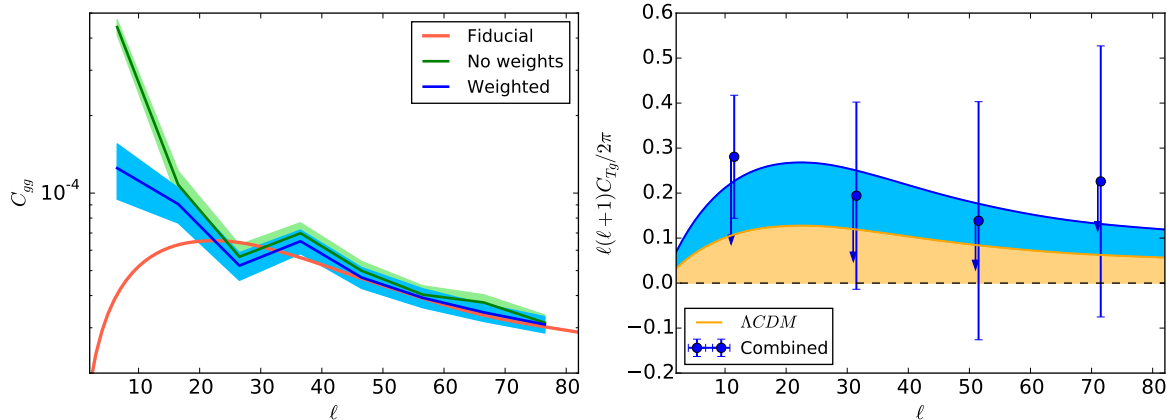


Figure 5. Left: the angular auto-power spectra of BOSS galaxies. The markers with error bars give the mean value in a bin of width $\Delta\ell = 10$. We show the measurement with and without the corrective weights for foreground systematics. Over-plotted with the red solid curve is a fiducial power spectrum computed with CLASS and halofit. We find that the data is consistent with a bias $b_g = 2.0$. Right, the cross galaxy-CMB temperature power spectrum. The fiducial model is over-plotted and we find a best fitting amplitude $\lambda = 2.4 \pm 1.0$. After subtracting the ISW map from the CMB, the cross-correlation drops, shown by the arrows.

5 CHARACTERISATION OF GRANESZ SUPER-STRUCTURES

5.1 Supervoid and supercluster profiles

The spectroscopic CMASS sample allows us to measure the shape and sizes of GraNeSz super-structures which were originally identified in a photometric redshift sample. We begin by measuring the number density of CMASS galaxies around the positions of GraNeSz super-structures. The catalogue includes 50 supervoids and 50 superclusters. We measure the mean density profile by taking the ratio of the number of galaxies to the normalised number of unclustered random points in a given separation bin. The number of points in the random catalogue is 17 times the total number of galaxies. Fig. 6 and 7 show the mean number density of the 50 supervoids and 50 superclusters as a function of distance parallel and perpendicular to the line-of-sight. We find that the profiles are not localised in the line-of-sight direction. This may be due to error in the individual centres estimated with photometric redshifts. To interpret these plots we will fit simple void and cluster profile models that includes uncertainty in the structure centre.

We estimate the variance of the profile measurements by generating many realisations centred on random positions in the survey. First, considering either the supervoid or supercluster catalogue, 50 random points are drawn from a random catalogue over the Northern field survey volume. Redshifts are assigned from the true redshifts in the superstructure catalogue. Then, the mean profile is measured from these positions. We used 1000 realisations of the process to estimate the diagonal elements of the covariance matrix for both supervoid and supercluster catalogues.

5.2 Void and cluster models

We use the following analytic form for the void profile with scale radius r_v and shape parameter α (Hawken et al, *in*

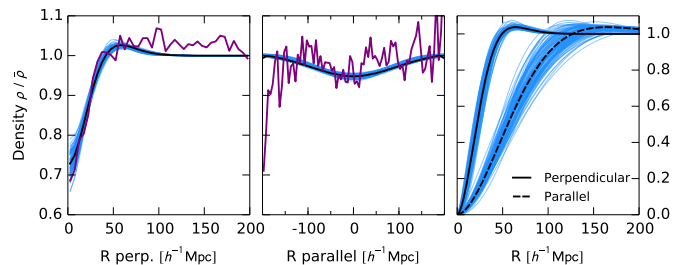


Figure 8. The GraNeSz supervoid profile (left) projected parallel to the line-of-sight, (center) projected perpendicularly to the line-of-sight, (right) the deconvolved three-dimensional model. The measurements are compared with the best-fit model (dark solid curve) and samples taken from the Markov chains (light blue curves).

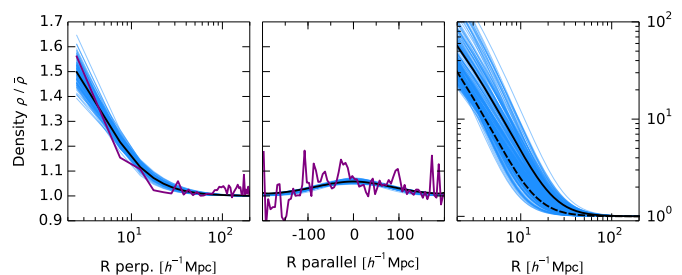


Figure 9. The same as Fig. 8, but for GraNeSz superclusters.

prep.):

$$\frac{\rho(\tilde{r})}{\bar{\rho}} = 1 - \left(1 - \frac{\alpha \tilde{r}^\alpha}{3r_v^\alpha}\right) \exp\left[-\left(\frac{\tilde{r}}{r_v}\right)^\alpha\right]. \quad (11)$$

The void is permitted to be elongated along the line-of-sight with ellipticity parameter q , and we define:

$$\tilde{r}^2 = r_{perp}^2 + r_{par}^2/q^2. \quad (12)$$

Superclusters are known to have irregular morphologies

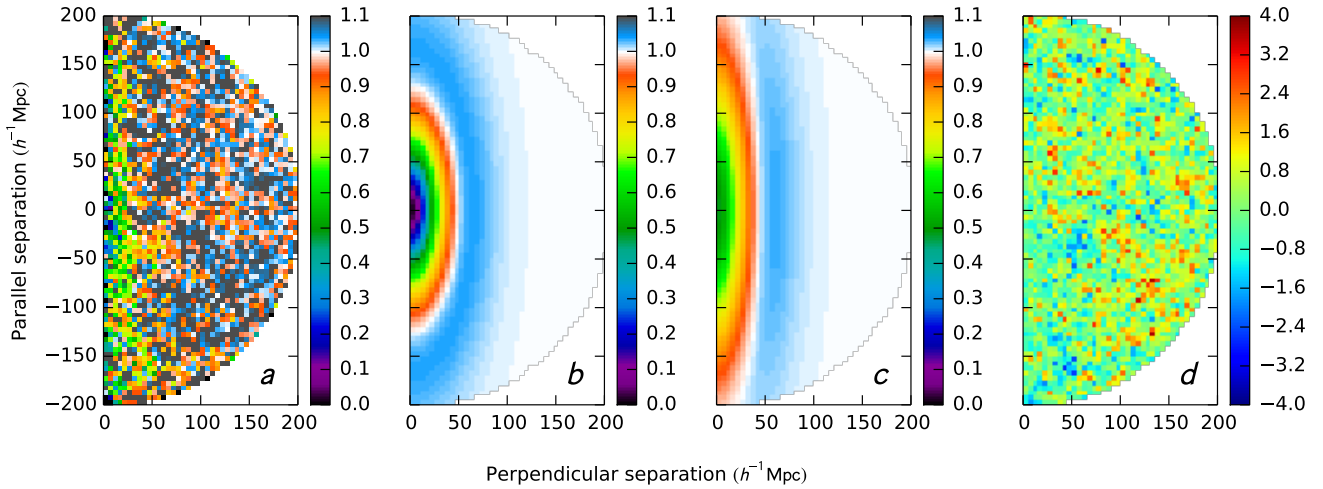


Figure 6. Mean GraNeSz supervoid profile: (a) the normalised number density of CMASS galaxies measured in bins perpendicular and parallel to the line-of-sight (bin size is $5h^{-1}\text{Mpc}$), (b) the best-fit model density profile of the void, (c) the model convolved with the best-fit Gaussian line-of-sight position error showing how it would appear in observations, (d) the residual in units of standard deviation after subtracting the convolved model from the data.

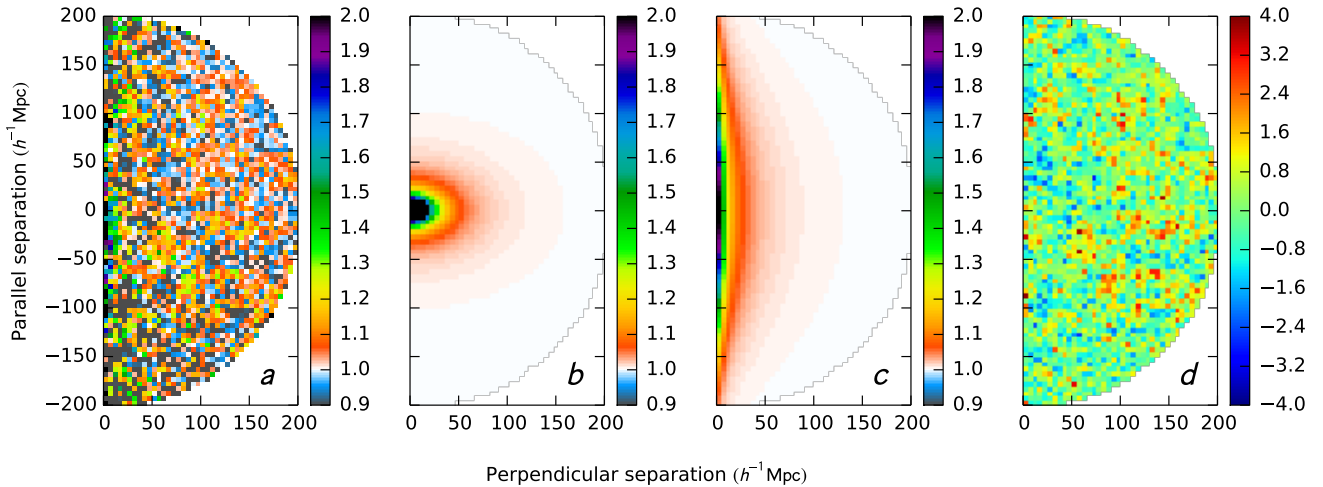


Figure 7. Same as Fig. 6, but for the GraNeSz supercluster catalogue.

(Einasto et al. 2014) and may not be well approximated by spherical symmetry. Nevertheless we apply the Navarro, Frenk & White (1996, NFW) analytic form to characterise the mean supercluster profile:

$$\frac{\rho(\tilde{r})}{\bar{\rho}} = 1 + \frac{\delta_c}{\tilde{r}(1 + \tilde{r}/r_s)^2} \quad (13)$$

The supercluster profile is also allowed to be elongated along the line-of-sight with parameter q .

We allow for a scatter in the line-of-sight position by introducing a convolution with a Gaussian kernel characterised with scale σ_{los} :

$$\rho_z(r_{perp}, r_{par}) = \frac{1}{\sqrt{2\pi\sigma_{los}^2}} \int e^{-\frac{(y-r_{par})^2}{2\sigma_{los}^2}} \rho(r_{perp}, y) dy. \quad (14)$$

We fit the model parameters to the measurements using a Markov chain monte carlo method implemented with the

Emcee package¹ (Foreman-Mackey et al. 2013). The fit is carried out using the diagonal covariance matrix constructed as described above.

We give the medians of the parameter chains along with the 68% confidence levels in Table 3. In Figs. 6 and 7 we show the mean anisotropic profiles of the voids and clusters along with the best-fit models with their residuals. The fit is carried out on the model convolved with the Gaussian kernel (Eq. 14) but we also show the profile before the convolution step to represent the underlying galaxy distribution. Figs. 8 and 9 compare the model with perpendicular and parallel projections of the profiles along with the model three-dimensional radial profile. The goodness of fit is $\chi^2_{void} = 0.93$ and $\chi^2_{cluster} = 0.99$ per degree of freedom for the supervoid and supercluster models respectively.

¹ <http://dan.iel.fm/emcee/>

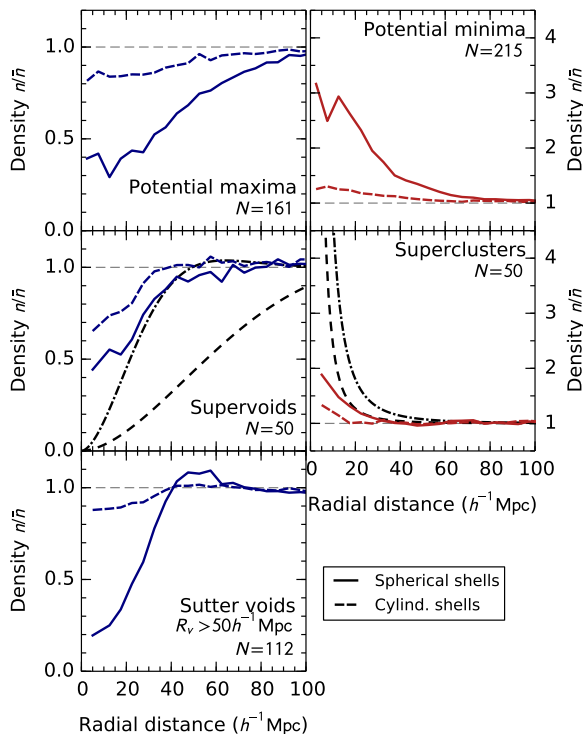


Figure 10. Radial density profiles of BOSS super-structures. Top row: local minima and maxima of the gravitational potential. Middle row: GraNeSz supervoids and superclusters. The best-fit models for the three-dimensional profile parallel (long-dashed curve) and perpendicular (dot-dashed curve) to the line-of-sight are shown. Bottom row: supervoids from the Sutter DR10 analysis. Plotted are profiles in spherical shells as well as cylindrical shells along the line of sight within $r = 200h^{-1}\text{Mpc}$ to show a representation of the structure in photometric redshift space.

In principle we could recenter each structure along the line-of-sight to correctly superpose the profiles. However, we found that due to the sparseness of the spectroscopic catalogue, the true centres could not be accurately estimated and so the uncertainty in the position can only be corrected for statistically on the mean profile.

5.3 Discussion

The model fits demonstrate that the supervoid and supercluster samples both represent large structures. The voids reach to $R = 50h^{-1}\text{Mpc}$ and the scale radius for superclusters is $r_s = 9h^{-1}\text{Mpc}$.

The mean supercluster profile is much broader than that which would be expected for a typical massive cluster. We find that the radius that encloses a mean density $200\rho_{crit}$ is $r_{200} = 1.1h^{-1}\text{Mpc}$ giving a concentration index $c_{200} \equiv r_s/r_{200}$ of $c_{200} = 0.12$ while massive clusters have concentration $c_{200} \approx 3$ (Umetsu et al. 2015). Given the low concentration index, the mass within r_{200} is modest: we find $M_{200} = 1.5 \times 10^{14}h^{-1}M_{\odot}$. If we instead integrate to the scale radius r_s we find $M(r < r_s) = 4.7 \times 10^{15}h^{-1}M_{\odot}$. For a typical massive cluster these masses are $M_{200} = 1 \times 10^{15}h^{-1}M_{\odot}$ and $M(r < r_s) = 2 \times 10^{14}h^{-1}M_{\odot}$. The scale of the superclus-

ters suggests that they are not virialized structures. Despite this, we find that the NFW profile characterises the mean profile well.

The best-fit void model is elongated along the line-of-sight with axis ratio $q = 2.6 \pm 0.4$. We found that a spherically symmetric model is unable to fit the data even with the free line-of-sight smoothing parameter. We explored this peculiarity with more general void profile forms, but found that even a spherically symmetric step function profile is unable to reproduce the measurement. On the other hand, the supercluster model is not strongly elongated: we find only a marginal squashing with q discrepant from unity at the 1σ level.

How can we interpret the apparent elongation of the supervoids? This is likely to be a real effect arising from the void-finding algorithm. GraNeSz identified the supervoids and superclusters in a photometric redshift catalogue with redshift error $\sigma_z \sim 0.05 \sim 100h^{-1}\text{Mpc}$. We suggest that when applied to a photometric sample the algorithm is most sensitive to under-dense tubes that are pointed along the line-of-sight. The effect is important for voids because they are large, irregularly shaped structures. Superclusters are also known to have wall-like or filamentary morphologies (Einasto et al. 2014); however, we find that the structures in the supercluster catalogue do not have a preferred alignment.

The void and cluster models incorporate the position uncertainty through the smoothing parameter σ_{los} . We found that the parameter is required to fit both the supervoid and supercluster measurements; moreover the scales determined from the two models are in excellent agreement. Interpreting this effect as arising from redshift error, the scale $\sigma_{los} = 76h^{-1}\text{Mpc}$ corresponds to a redshift error of $\sigma_z = 0.034$.

6 COMPARISON OF BOSS SUPER-STRUCTURES

6.1 Local extrema of the gravitational potential

We construct a new superstructure catalogue defined by the positions of local extrema of the gravitational potential field. The starting point is the Wiener estimate of the gravitational potential derived through the Poisson equation, Eq. 2. We perform the computation on a grid with cell size $10h^{-1}\text{Mpc}$, thus we may resolve structures on scales $R > 20h^{-1}\text{Mpc}$. To find the largest structures, we convolve the field with a three-dimensional Gaussian filter with full-width half-maximum $60h^{-1}\text{Mpc}$. The local extrema of the field then correspond to cells that are more extreme, either greater or less than, their six adjacent cells. The positions of the extrema are discretised by the grid. This introduces an uncertainty of $10h^{-1}\text{Mpc}$ which corresponds to an angular scale of ~ 30 arcmin; however, this uncertainty in the structure positions is much less than the smoothing scale. Minima of the potential correspond to over-densities, while maxima correspond to under-densities in the galaxy field. We exclude objects with centres less than 10° from the survey boundary. We find 136 and 25 supervoids in the North and South, respectively, and 166 and 49 superclusters in the North and South, marked in Fig. 4.

6.2 Radial density profiles

In Fig. 10 we compare the radial density profiles of three super-structure catalogues: GraNeSz, peaks and troughs of the potential and the DR10 spectroscopic void catalogue by Sutter et al. (2014). The projected profiles are computed by averaging in cylinders along the line-of-sight within a sphere of $r = 200h^{-1}\text{Mpc}$. In the case of the GraNeSz structures the void centres are given by the photometric redshift estimates, but we overplot the deconvolved best-fit model found in Sec. 5.2. The Sutter voids were selected in the redshift range $0.5 < z < 0.6$ and have radii $R > 50h^{-1}\text{Mpc}$. We found that for voids with radius less than $40h^{-1}\text{Mpc}$ the structures in projection are overdensities, a fact pointed out by (Nadathur & Hotchkiss 2014; Cai et al. 2014). We find that the GraNeSz voids are deeper in projection than the Sutter voids, reinforcing the fact that photometric and spectroscopic void finders can be sensitive to different types of structures.

The superstructures identified from local extrema of the gravitational potential appear significantly larger in extent. The supervoids appear significantly underdense, deeper than GraNeSz supervoids and match the depth of Sutter et al. (2014) catalogue, but lacking the compensated ring structure. Moreover, in projection they appear deeper than the GraNeSz voids. The superclusters are found to be significantly more dense than GraNeSz superclusters, both in three-dimensions and projection.

6.3 Radial temperature profiles

We now examine the imprint of these structures in our model ISW map and in the Planck temperature map. We will use the ISW map as a template to match to the CMB data. The radial ISW temperature profiles are shown in the left column of Fig. 11 and the temperature profiles on the CMB are shown on the right. The shaded regions show the 68 and 95% confidence intervals. For the ISW map, the confidence interval was determined by measuring the profile around randomly distributed points within the survey mask. We use 1000 random realisations to compute the variance of the profile in this way. On the right, for the variance on the CMB temperature, we keep the coordinates of the structures fixed and generate mock CMB skies using the Healpix Synfast code. Here we also use 1000 realisations and compute the covariance matrices for the profiles.

The amplitude of the profile is affected by long-wavelength fluctuations that effectively modulate the background level. To remove this variance we apply a high-pass filter to both the ISW and CMB maps. We use a filter with a cosine cut-off at $\ell = 10$, corresponding to 20° scales. In presenting the profile, we further subtract the mean temperature at 10° scales. We do not expect such filtering to affect a well-localised signal arising from individual voids or clusters.

We see that each super-structure sample is correlated with the ISW map to some degree. The peaks and troughs of the potential have the largest amplitude, which can be expected by their construction. The GraNeSz sources do not correspond to the most extreme features in the map, but show significant correlation. On the other hand, the Sutter et al. (2014) sample shows only a weak correlation with the

Sample	N	λ	σ	λ/σ
GraNeSz supervoids	50	6.30	2.59	2.4
GraNeSz superclusters	50	4.51	3.57	1.3
Potential minima	215	0.23	0.59	0.4
Potential maxima	161	0.61	1.05	0.6
Sutter DR10	112	1.23	5.39	0.2

Table 4. ISW source template fit significances.

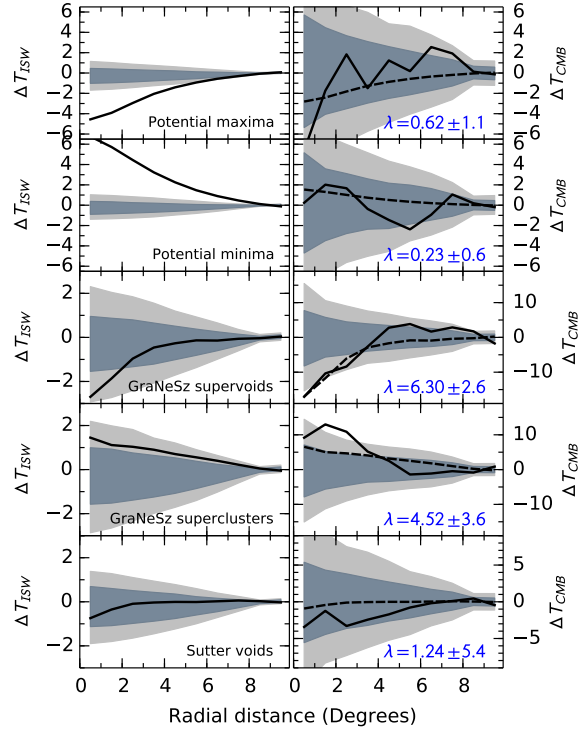


Figure 11. Mean temperature profiles of super-structure catalogues. Left: the profile of structures projected on the ISW map; right: the measured temperature profile on the CMB. The shaded regions show 68% and 95% confidence intervals.

ISW map, which may be anticipated by their shallow profiles in projection.

We use the ISW profile measured on the ISW map as a template to fit the CMB temperature profile. The template fit statistic and variance are computed as given by Eqs. 6 and 7. The resulting significances are listed in Table 4. We find marginal detections of the GraNeSz supervoids and superstructures. The supervoid sample gives higher significance than the supercluster because there is better agreement between the measured profile and the template shape. For the other samples the fits are consistent with no correlation.

7 CONCLUSIONS

The BOSS survey volume and sampling rate allow a detailed investigation of ISW sources at redshift $z = 0.5$. We have used the spectroscopic sample to further investigate

the GraNeSz super-structure catalogue and carried out a preliminary analysis of public catalogues. Our main findings may be summarised as follows.

- We constructed a map of the ISW anisotropy sourced by CMASS galaxies and confirmed that the signal is present in the CMB temperature map at the 97% confidence level. The detection is not significant in the Southern field. This may be due to the small area and intrinsic variance of the signal or contamination by strong foreground systematics in the South.
- We demonstrated that the signal is consistent with the measured galaxy density - temperature cross-correlation function with similar North-South differences.
- We carry out a detailed characterisation of the GraNeSz super-structures. We confirm that they are indeed vacuous supervoids and extensive superclusters, but they are not well localised in the line-of-sight direction. We model this uncertainty as a convolution of the profile. Fitting the model to the observed mean profile, we find that the supervoids are intrinsically elongated along the line-of-sight. We suggest that this feature arises from the void-finding algorithm run on a photometric redshift sample.
- We construct a new super-structure catalogue based upon peaks and troughs of the gravitational potential. These structures have a much larger extent than the GraNeSz and Sutter et al. (2014) objects, and should be expected to give a strong linear ISW contribution.
- We compare the mean radial density profiles of structures and find that Sutter et al. (2014) voids are relatively shallow in projection owing to the compensated shell. The voids found with photometric redshifts do not show this morphology.
- We construct ISW signal templates for the superstructure catalogues based upon our ISW map. We use the template as a filter on the CMB to measure the ISW contribution, largely free of ‘look elsewhere’ bias. With this method we find marginal detections of the GraNeSz super-structures, but the other super-structure samples are consistent with no signal.

We have resolved remaining questions regarding the nature of the GraNeSz super-structures by quantifying their morphologies; however, their apparent imprint on the CMB remains unexplained. The elongation of the voids may offer a clue: we expect that the extreme tail of the ISW signal is sourced by structures that happen to be elongated along the line-of-sight (Flender, Hotchkiss & Nadathur 2013). However, the linear ISW signal that we estimate based upon the reconstructed potential does not account for the measured temperature anisotropy. Moreover our analyses of other super-structure catalogues give results fully consistent with the expectation in the Λ CDM model. Thus we are unable to confirm the existence of anomalous ISW sources.

The approach we have developed here is fully empirical: we can characterise the sources expected to contribute most strongly to the ISW signal. However there is also an important need for theoretical expectations that can be provided by N-body simulations. The picture may come into focus with future refinements of super-structure catalogues in BOSS. We also look to upcoming photometric and spectroscopic surveys to improve the fidelity of the galaxy density field reconstructions on large scales.

APPENDIX A: COMPARISON WITH PHOTOMETRIC ISW MAP

We have probed the ISW signal over the same area of sky and in a similar redshift range as an earlier work by Granett, Neyrinck & Szapudi (2009). This previous study used a photometric sample of luminous red galaxies in the redshift range $0.4 < z_{\text{phot}} < 0.6$ based on photometric redshifts. Since the integrated linear signal depends on the redshift of the sources only weakly through the growth factor we expect that maps generated with photometric or spectroscopic redshifts should be equivalent. The maps from the two works are shown in Fig. A1. By eye we can find some correspondence between the two maps for instance the hot spot in the top left at RA, dec. 210° , 50° is in common; however, the large-scale fluctuations do not appear to match up.

For quantitative comparison we compute the correlation coefficient of the spherical harmonic decompositions of the two maps A and B indexed by ℓ : $r_\ell = C_\ell^{AB} / \sqrt{C_\ell^A C_\ell^B}$ plotted in the bottom panel of Fig. A1. On large scales we find an anti-correlation with $r < 0$. The correlation becomes positive at $\ell > 10$ (20° scales) with $r \sim 0.6$. The mean correlation between the two maps is $r = 0.2$. As a sanity-check we flip one of the maps in right ascension and repeat the measurement. This results in a reduced correlation coefficient as shown by the dashed curve in the figure.

We find that the two maps are correlated on small scales at the 60% level but it is not perfect. This may be explained by the noise properties of the samples: the photometric survey has a greater density of galaxies and so gives an estimate with reduced shot noise. Furthermore, the redshift distributions of the samples do differ.

ACKNOWLEDGMENTS

We thank Simone Aiolo, Seshadri Nadathur, Mark Neyrinck and István Szapudi for discussing this work with us. BRG and AJH acknowledge support of the European Research Council through the Darklight ERC Advanced Research Grant (# 291521). AK was supported by the Spanish Ministerio de Economía y Competitividad (MINECO) under projects FPA2012-39684, and Centro de Excelencia Severo Ochoa SEV-2012-0234.

The results were derived with CosmoPy (www.ifa.hawaii.edu/cosmopy) and Healpix with Healpy (healpix.jpl.nasa.gov, code.google.com/p/healpy).

Funding for SDSS-III has been provided by the Alfred P. Sloan Foundation, the Participating Institutions, the National Science Foundation, and the U.S. Department of Energy Office of Science. The SDSS-III web site is <http://www.sdss3.org/>. SDSS-III is managed by the Astrophysical Research Consortium for the Participating Institutions of the SDSS-III Collaboration including the University of Arizona, the Brazilian Participation Group, Brookhaven National Laboratory, Carnegie Mellon University, University of Florida, the French Participation Group, the German Participation Group, Harvard University, the Instituto de Astrofísica de Canarias, the Michigan State/Notre Dame/JINA Participation Group, Johns Hopkins University, Lawrence Berkeley National Laboratory, Max Planck Institute for Astrophysics, Max Planck Institute for Extraterrestrial Physics, New Mexico State University, New York University, Ohio State University, Pennsylvania State University, University of Portsmouth, Princeton University, the Spanish Participation Group, University of Tokyo, University of Utah, Vanderbilt University, University of Virginia, University of Washington, and Yale University.

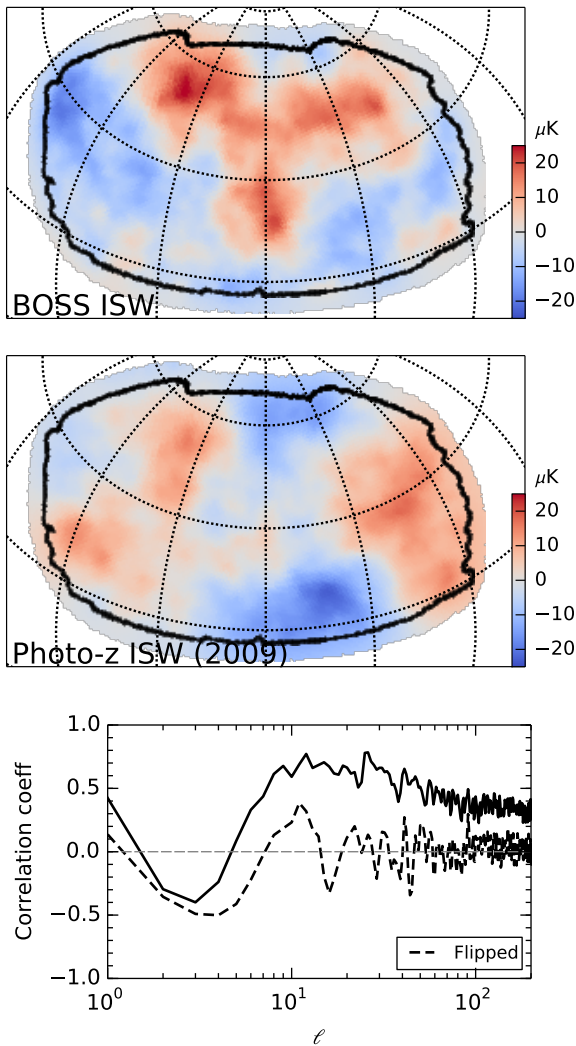


Figure A1. A comparison of the ISW map derived in this work (top frame) with the map estimated using a photometric sample of luminous red galaxies from Granett, Neyrinck & Szapudi (2009) (middle frame). The correlation coefficient between the two maps is plotted in the bottom frame as a function of harmonic multipole ℓ (solid line). The dashed line shows the result after flipping one of the maps in right ascension.

REFERENCES

- Afshordi N., 2004, PRD, 70, 083536
 Afshordi N., Tolley A. J., 2008, PRD, 78, 123507
 Aiola S., Kosowsky A., Wang B., 2015, PRD, 91, 043510
 Alam S. et al., 2015, ApJ Supplement, 219, 12
 Anderson L. et al., 2014, MNRAS, 441, 24
 Bolton A. S. et al., 2012, AJ, 144, 144
 Cabré A., Gaztañaga E., 2009, MNRAS, 396, 1119
 Cai Y.-C., Cole S., Jenkins A., Frenk C. S., 2010, MNRAS, 407, 201
 Cai Y.-C., Neyrinck M. C., Szapudi I., Cole S., Frenk C. S., 2014, ApJ, 786, 110
 Chon G., Challinor A., Prunet S., Hivon E., Szapudi I., 2004, MNRAS, 350, 914
 Crittenden R. G., Turok N., 1996, Physical Review Letters,

76, 575

- Einasto M., Lietzen H., Tempel E., Gramann M., Liivamägi L. J., Einasto J., 2014, A&A, 562, A87
 Flender S., Hotchkiss S., Nadathur S., 2013, J. Cosmol. Astropart. Phys., 2, 13
 Foreman-Mackey D., Hogg D. W., Lang D., Goodman J., 2013, PASP, 125, 306
 Francis C. L., Peacock J. A., 2010, MNRAS, 406, 14
 Frommert M., Enßlin T. A., 2009, MNRAS, 395, 1837
 Giannantonio T., Martinelli M., Silvestri A., Melchiorri A., 2010, J. Cosmol. Astropart. Phys., 4, 30
 Giannantonio T., Ross A. J., Percival W. J., Crittenden R., Bacher D., Kilbinger M., Nichol R., Weller J., 2014, PRD, 89, 023511
 Giannantonio T., Scranton R., Crittenden R. G., Nichol R. C., Boughn S. P., Myers A. D., Richards G. T., 2008, PRD, 77, 123520
 Górski K. M., Hivon E., Banday A. J., Wandelt B. D., Hansen F. K., Reinecke M., Bartelmann M., 2005, ApJ, 622, 759. <http://healpix.jpl.nasa.gov/>
 Granett B. R., Neyrinck M. C., Szapudi I., 2008, ApJ Letters, 683, L99
 —, 2009, ApJ, 701, 414
 Granett, B. R. et al., 2015, A&A, 583, A61. <http://dx.doi.org/10.1051/0004-6361/201526330>
 Hernández-Montegudo C. et al., 2014, MNRAS, 438, 1724
 Hernández-Montegudo C., Smith R. E., 2013, MNRAS, 435, 1094
 Ho S. et al., 2012, ApJ, 761, 14
 Ho S., Hirata C., Padmanabhan N., Seljak U., Bahcall N., 2008, PRD, 78, 043519
 Hotchkiss S., Nadathur S., Gottlöber S., Iliev I. T., Knebe A., Watson W. A., Yepes G., 2015, MNRAS, 446, 1321
 Ilić S., Douspis M., Langer M., Pénin A., Lagache G., 2011, MNRAS, 416, 2688
 Ilić S., Langer M., Douspis M., 2013, A&A, 556, A51
 Kovács A., Granett B. R., 2015, MNRAS, 452, 1295
 Manzotti A., Dodelson S., 2014, PRD, 90, 123009
 Maturi M., Dolag K., Waelkens A., Springel V., Enßlin T., 2007, A&A, 476, 83
 Nadathur S., Hotchkiss S., 2014, MNRAS, 440, 1248
 Nadathur S., Hotchkiss S., Sarkar S., 2012, J. Cosmol. Astropart. Phys., 6, 42
 Nadathur S., Lavinto M., Hotchkiss S., Räsänen S., 2014, PRD, 90, 103510
 Navarro J. F., Frenk C. S., White S. D. M., 1996, ApJ, 462, 563
 Neyrinck M. C., 2008, MNRAS, 386, 2101
 Neyrinck M. C., Gnedin N. Y., Hamilton A. J. S., 2005, MNRAS, 356, 1222
 Nishizawa A. J., 2014, Progress of Theoretical and Experimental Physics, 2014, 060000
 Peacock J. A., Dodds S. J., 1994, MNRAS, 267, 1020
 Peiris H. V., 2014, in IAU Symposium, Vol. 306, IAU Symposium, pp. 124–130
 Planck Collaboration et al., 2015a, ArXiv e-prints
 —, 2015b, ArXiv e-prints
 —, 2015c, ArXiv e-prints
 Raccanelli A., Kovetz E., Dai L., Kamionkowski M., 2015, ArXiv e-prints
 Rassat A., Starck J.-L., Dupé F.-X., 2013, A&A, 557, A32
 Rees M. J., Sciama D. W., 1968, Nature, 217, 511

- Ross A. J. et al., 2012, MNRAS, 424, 564
Sachs R. K., Wolfe A. M., 1967, ApJ, 147, 73
Sawangwit U., Shanks T., Cannon R. D., Croom S. M.,
Ross N. P., Wake D. A., 2010, MNRAS, 402, 2228
Sutter P. M., Pisani A., Wandelt B. D., Weinberg D. H.,
2014, MNRAS, 443, 2983
Swanson M. E. C., Tegmark M., Hamilton A. J. S., Hill
J. C., 2008, MNRAS, 387, 1391
Szapudi I. et al., 2015, MNRAS, 450, 288
Takahashi R., Sato M., Nishimichi T., Taruya A., Oguri
M., 2012, ApJ, 761, 152
Umetsu K., Zitrin A., Gruen D., Merten J., Donahue M.,
Postman M., 2015, ArXiv e-prints
Zibin J. P., 2014, ArXiv e-prints